ACS Catalysis

pubs.acs.org/acscatalysis
Research Article

Interrogation of the Interfacial Energetics at a Tantalum Nitride/Electrolyte Heterojunction during Photoelectrochemical Water Splitting by *Operando* Ambient Pressure X-ray Photoelectron Spectroscopy

Øystein Dahl, Martin Fleissner Sunding, Veronica Killi, Ingeborg-Helene Svenum, Mathieu Grandcolas, Magnus Andreassen, Ola Nilsen, Annett Thøgersen, Ingvild Julie Thue Jensen,* and Athanasios Chatzitakis*

Cite This: *ACS Catal.* 2023, 13, 11762−11770
Read Online

ABSTRACT: Photoelectrochemical (PEC) water electrolysis is an important energy conversion (power-to-chemical) method, providing a solution to the intermittent nature of solar energy. However, as PEC systems usually suffer from low operational stability, they are seriously lagging in up-scaled demonstrations and viability. PEC systems are based on semiconductor/liquid interfaces, which have been extensively studied by experiments and theory, but there is a significant knowledge gap in the energetics of such interfaces during operation. In this work, *operando* ambient pressure X-ray photoelectron spectroscopy (AP-XPS) has been used to characterize the electrical and spectroscopic properties of a pristine Ta_3N_5 photoelectrode and a Ta_3N_5/NiO_x protection/passivation layer system, which stabilizes an otherwise quickly corroding pristine photoelectrode. We directly observed Fermi-level pinning of Ta_3N_5 within the applied potential window under both dark and illumination conditions, detrimental to the performance and stability of the photoelectrode. Interestingly, in the Ta_3N_5/NiO_x protection/passivation layer system, the Fermi level gets unpinned under illumination, allowing quasi-Fermi-level splitting and sustaining a significant PEC performance as well as high stability.

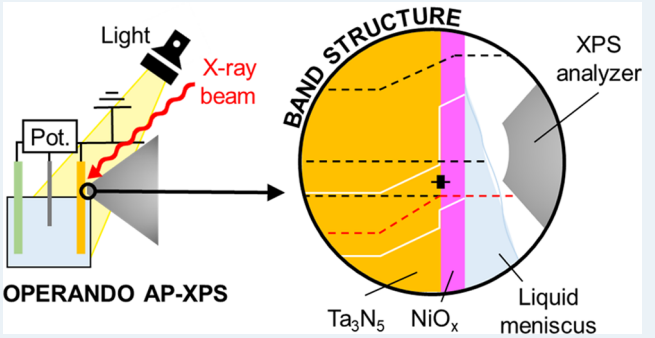

KEYWORDS: *operando, ambient pressure XPS, photoelectrochemical water splitting, tantalum nitride, interfaces, heterojunction, ALD, passivation*

1. INTRODUCTION

Photoelectrochemical (PEC) water electrolysis celebrated recently its 50th anniversary since the seminal work presented by Honda and Fujishima.[1] The interest in this technology is enormous, as well as the amount of work focusing on discovering new photocatalytic materials and improving the properties of the most common photocatalysts, such as TiO_2, Fe_2O_3, $BiVO_4$, and others.[2,3] Yet, there is still no commercial demonstration, and this is due to the stringent requirements for the photocatalytic material that at the same time must absorb light and perform catalysis. Photocatalytic materials must possess appropriate band structure, stability, and good kinetics for the oxygen evolution reaction (OER, photoanodes) or the hydrogen evolution reaction (HER, photocathodes).

The development of *operando* measuring conditions for analytical techniques, as in the case of ambient pressure X-ray photoelectron spectroscopy (AP-XPS), has enabled a more fundamental understanding of interfacial phenomena because they enable the interrogation of the material under operating conditions.[4−8] This is of paramount importance to the field of PEC water electrolysis as the band structure of a photocatalytic, semiconducting material in contact with an electrolyte (biased and not) is not the same as that in vacuum. The space charge region (SCR) forming (depletion region for an n-type semiconductor) under equilibrium conditions in the solid/liquid junction is a key factor for the transport of photogenerated holes from the solid to the surface of the photoanode electrode. The SCR and ultimately the band structure of a photocatalyst can be further altered between dark

Received: May 29, 2023
Revised: August 4, 2023
Published: August 22, 2023

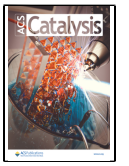

and illuminated conditions and when there is application or not of external bias. Thus, the band bending at the interface between the solid and electrolyte, especially under operating conditions, is a crucial parameter to investigate in order to understand the PEC performance of photoelectrode materials. Under ultrahigh vacuum (UHV) conditions as in a standard XPS analysis chamber, the water vapor partial pressure is very low (typically 1×10^{-8} mbar), and the surface band bending (if any) toward the surface in vacuum cannot be extrapolated to give information about the band bending during PEC operation. As a result, measurements in UHV cannot probe the interfacial energetics of the semiconductor/electrolyte junction and are exclusively limited to pre- and postoperation conditions. Insufficient understanding of the interfacial energetics during operation is among the main reasons for the slow development of PEC water electrolysis, and we will address it in this work.

Among the most promising photocatalytic materials serving as photoanodes is tantalum nitride (Ta_3N_5), which has a band-gap energy of approximately 2.2 eV and suitably placed valence and conduction band energy levels (VBE and CBE).[9,10] Compared to hematite, which has a similar band-gap energy but not suitable VBE and CBE for water photoelectrolysis, Ta_3N_5 can easily achieve photocurrent densities exceeding 6 mA/cm^2 at 1.23 V vs the reversible hydrogen electrode (RHE)[11] and, in some cases, even reaching close to its theoretical performance of approximately 13 mA/cm^2 at 1.23 V vs RHE.[12,13] The key challenge is its instability as Ta_3N_5 self-oxidizes by the photogenerated holes forming an oxynitride-rich surface, as well as the formation of deep trap centers (Ta^{3+}) that are detrimental to its PEC performance.[14,15] Several cocatalysts, such as NiFe, CoO_x, Co-Pi, and others, have been applied in order to not only protect the underlying Ta_3N_5 but also increase the OER kinetics, mainly in strongly alkaline conditions (1 M KOH).[12,16,17] Additional buffer layers, as well as hole- and electron-extracting layers inspired by the photovoltaic (PV) community, have been applied but still the stability is rather poor.[18] A possible reason is pinhole formation or insufficient coverage of the surface of Ta_3N_5 by the protective layers and cocatalysts. On the other hand, Zhao and co-workers have shown an impressive performance with a 120 h long stable PEC operation at high current densities.[19] In this case, Ta_3N_5 was coated by atomic layer deposition (ALD) with an AlO_x dielectric layer and a hole storage layer of ferrihydrite (Fh). The protected electrode was then coated with another layer consisting of $NiFeO_x/CeO_x$ as the cocatalyst for the OER. Although this work showcases a leap into the stabilization of Ta_3N_5, the underlying mechanism is still unknown, especially when it comes to the band structure and energetics of the formed interfaces.

In this work, we investigate the interfacial phenomena occurring during the contact of photoelectrodes based on Ta_3N_5 thin films (both as-prepared and NiO_x-coated by ALD) with electrolyte (1 M KOH) by *operando* AP-XPS. It is well-known that NiO_x is an efficient OER catalyst in alkaline electrolytes; therefore, our main hypothesis is that NiO_x can both protect the underlying Ta_3N_5 photocatalyst and act as a cocatalyst that catalyzes the OER by effectively extracting photogenerated holes from Ta_3N_5. During *operando* AP-XPS, we monitor the kinetic energy of photoelectrons emitted from the semiconductor/electrolyte interface under bias in dark and illuminated conditions. The goal of our work is to interrogate the Ta_3N_5/electrolyte and Ta_3N_5/NiO_x/electrolyte heterojunctions during operation, ultimately identifying the governing principles of Ta_3N_5 degradation. He et al. suggested based on *ex situ* XPS studies that Fermi-level (E_F) pinning suppresses the photoactivity of the material.[14] Herein, we confirm this behavior for the as-prepared Ta_3N_5 thin film using *operando* AP-XPS. For the NiO_x-coated Ta_3N_5, on the other hand, we observe that the E_F in NiO_x-coated Ta_3N_5 is still pinned in the dark condition, but under illumination, we find that quasi-Fermi-level unpinning is allowed and the photoactivity of Ta_3N_5 is maintained, thus suppressing degradation. These key findings directly probed in operating conditions provide fundamental insights into the underlying mechanisms that can accelerate the development of robust materials for a viable and competitive PEC water electrolysis systems.

2. EXPERIMENTAL SECTION

2.1. Synthesis of Ta_3N_5 Film Electrodes. Ta_3N_5 thin films were prepared by first depositing a metallic Ta film by sputtering it on fused silica slides. Sputtering was performed in a nanoPVD instrument in DC mode (DC PSU% = 10, Ar flow = 10 sccm, room temperature, pre-deposition chamber pressure <2 × 10^{-6} mbar) for 60 min. The deposited Ta metal films were then annealed in an NH_3 atmosphere for 8 h at 950 °C with a heating ramp rate of 10 °C/min. As the fused silica substrate is nonconductive, Ag (LOCTITE MR3863 Circuit+) contacts were hand-painted forming a frame as seen in Figure S1. The Ag contacts were then covered and insulated with epoxy resin (Araldite).

2.2. Synthesis and Deposition of NiO_x on Ta_3N_5 Film Electrodes (Ta_3N_5/NiO_x) through ALD. Ta_3N_5/NiO_x photoelectrodes were synthesized by a direct growth of a thin NiO_x layer on Ta_3N_5 film electrodes with ALD using a process based on the work of Lindahl et al.[20] The films were deposited in a flow-type ALD reactor (F-120 Sat, ASM Microchemistry Ltd.) using resublimed $Ni(thd)_2$ (Volatec) and water (type 2) as precursors and nitrogen (<99,999%, PRAXAIR) as a carrier gas. The $Ni(thd)_2$ was sublimed at 130 °C in the reactor, while water was delivered at room temperature. The reaction temperature was 230 °C, and a pulsing scheme was 3−8−4.5−8 s of pulse $Ni(thd)_2$−purge−pulse water−purge. The average growth rate on tokens of Si(100) wafer was ca. 0.04 Å/cycle, significantly lower than the 0.32 Å/cycle reported in ref 20. The reasons for the reduced growth rate are unknown but were taken into consideration when designing the depositions.

2.3. *Operando* AP-XPS Characterization. AP-XPS measurements were performed at the HIPPIE beamline at the MAX IV synchrotron in Lund, Sweden, using the "dip and pull" setup.[4] The setup consisted of the pristine Ta_3N_5 and the ALD-coated NiO_x Ta_3N_5 photoanodes (working electrode, WE), a Pt sheet (2 cm^2) as the cathode (counter electrode, CE), and Ag/AgCl (3.4 M KCl, leakless miniature reference electrode model ET072) as the reference electrode (RE) in a custom-made beaker containing 1 M KOH as the electrolyte inside the AP-XPS analysis chamber. A simplified schematic of the "dip and pull" setup in the ambient pressure analysis chamber of XPS is shown in Figure 1.[4,21] By the method's principle, the WE was grounded to the spectrometer to ensure a common energy reference during the photoemission measurements. The PEC measurements were controlled by an Ivium Vertex potentiostat/galvanostat. The sample was illuminated through a view port by using a solar simulator (ASAHI HAL-320 300W). The light intensity from the

https://doi.org/10.1021/acscatal.3c02423
ACS Catal. 2023, 13, 11762−11770

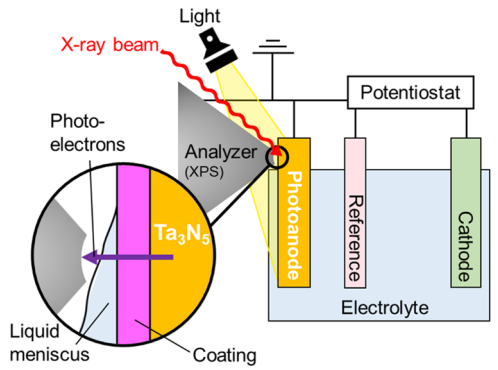

Figure 1. Schematic representation of the "dip and pull" setup in the ambient pressure condition analysis chamber. A liquid meniscus forms when the sample is dipped and pulled out slowly from the electrolyte solution. The solution is in equilibrium with its vapor pressure in the chamber. The working electrode (WE) is grounded to the analyzer (cone) to equalize the Fermi energy level of the detector with the contact of the WE. The reference (RE) and counter electrodes (CE) are used to control the potentials in the experiments with the use of a potentiostat. Simulated solar light was supplied externally through a view port.

condensing lens of the solar simulator to the surface of the electrode through the view port was measured to be between 0.2 and 0.3 suns with a calibrated reference Si PV cell (Newport, model 91150 V). This was advantageous in order to operate at low photocurrent density (a few $\mu A/cm^2$) and match the relatively long AP-XPS acquisition times (approximately 1 h at each applied potential) and the fast photocorrosion rate of such films (complete loss of photoactivity after typically 10 min[22]). Excessive oxygen gas evolution on the electrode that could interfere with the AP-XPS data acquisition through the meniscus is also avoided. All potentials are reported and corrected against the reversible hydrogen electrode (RHE) as described in the additional experimental procedures given in the Supporting Information (SI). It is also highlighted that the Ag/AgCl reference electrode was checked against a master reference electrode (saturated calomel electrode (SCE)). In the "dip and pull" measurement, when the position of the beaker is slightly lowered, a thin meniscus of electrolyte is formed on the WE's surface that allows for XPS measurement of the solid/liquid (photoanode/electrolyte) interface. The beam energy was 1800 eV, and the photoelectrons were collected in normal emission from the sample surface. Reference measurements of the Ta 4f, C 1s, N 1s, O 1s, and valence regions were performed under vacuum (pressure: $\sim 10^{-5}$ mbar). For the *operando* data acquisition (pressure: 15−20 mbar), the measurement of the Ta 4f and O 1s regions was prioritized, as they provide the necessary information for Ta_3N_5 and the water meniscus. The signals from N 1s and Ni 2p were too weak to be compatible with the *operando* measurements. In order to avoid beam damage, Ta 4f and O 1s spectra were measured repeatedly while continuously moving the sample in the horizontal direction along the meniscus edge with a speed of 2.5 μm/s. The range of feasible meniscus thicknesses, i.e., thin enough for XPS measurements of the solid/liquid interface while thick enough to preserve electrical contact with the electrolyte in the beaker, was quite narrow. Furthermore, the thickness of the electrolyte meniscus was not uniform in the horizontal direction due to the textured surface of the samples. This was handled by using the relative intensity of the O 1s gas and liquid components to adjust the measurement position up or down in the vertical direction on the fly. Additionally, the data was postprocessed to remove points with insufficient electrical contact with the electrolyte or excess electrolyte thickness as described in Supplementary Note 1. XPS data was collected from fresh areas of the anode for each applied bias point by dipping the sample ~100 μm deeper between each bias series.

3. RESULTS

3.1. PEC Performance. Figure 2 shows the PEC performance in 1 M KOH under 1 sun simulated illumination of the Ta_3N_5 and Ta_3N_5/NiO_x samples.

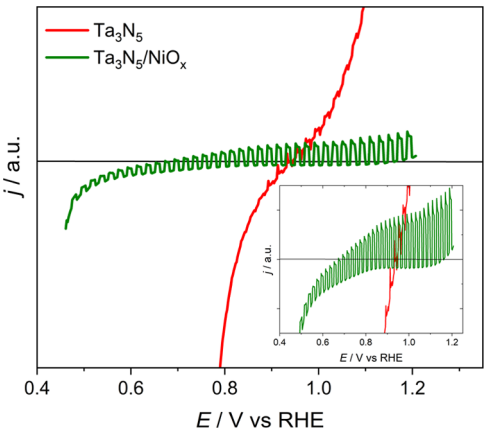

Figure 2. Linear sweep voltammograms in 1 M KOH, showing the effect of the NiO_x film on the PEC performance of Ta_3N_5. A scan rate of 10 mV/s and scan direction from less positive to more positive potentials were applied. The inset shows a higher magnification, highlighting the performance difference. Zero current position is denoted by a black solid line.

The Ta_3N_5 sample is characterized by significant dark currents, which are related to oxidation and reduction processes of the materials itself.[23,24] The photocurrent generation is also extremely limited and heavily obscured by the dominant dark currents. In contrast, when Ta_3N_5 is coated by a NiO_x layer, we observe that the dark currents are heavily suppressed in a large potential window ranging from +0.60 to +1.23 V vs RHE. Moreover, the photoactivity of the material is heavily improved as seen by the significant generation of photocurrent with small photocurrent spikes, implying an improved charge carrier separation. Macroscopically then, the effect of the protective and cocatalyst acting NiO_x layer has an enormous effect on the PEC performance of Ta_3N_5. Detailed physicochemical characterization including TEM−EDS, XRD, and transmission measurements can be found in the SI (Figures S2−S4). Below, we unravel the underlying mechanisms of the observed PEC performance by *operando* measurements and detailed characterizations on the nanoscale.

3.2. XPS Characterization of Ta_3N_5 and Ta_3N_5/NiO_x. Figure 3 shows XPS reference spectra taken under vacuum conditions for Ta_3N_5 and Ta_3N_5/NiO_x prior to the *operando* AP-XPS experiments. The Ta 4f and N 1s spectra from the Ta_3N_5 phase are similar for both samples with the Ta $4f_{7/2}$ and Ta $4f_{5/2}$ at binding energies of 24.6 and 26.5 eV, respectively. The corresponding N 1s contribution of Ta_3N_5 is at 396.4 eV in agreement with the literature,[25] and the broad contribution around 403.3 eV is associated with Ta $4p_{3/2}$. The O 1s region

https://doi.org/10.1021/acscatal.3c02423
ACS Catal. 2023, 13, 11762−11770

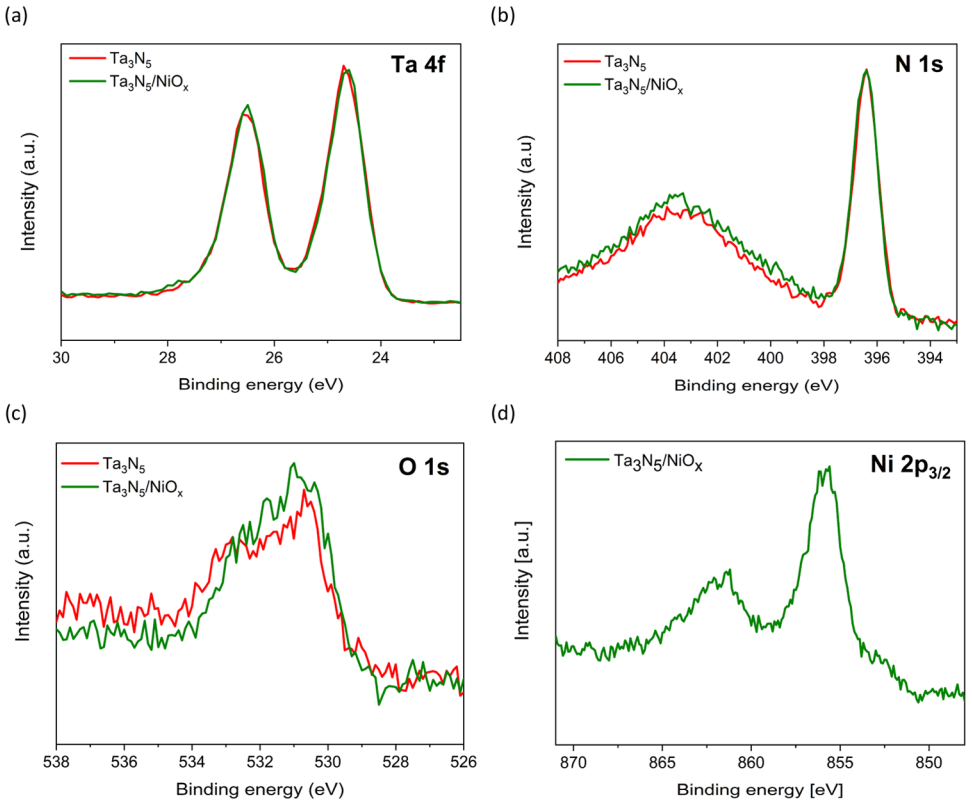

Figure 3. XPS spectra of Ta_3N_5 (red) and Ta_3N_5/NiO_x (green) taken under vacuum conditions at the HIPPIE beamline by using a photon energy of 1800 eV. (a) Ta 4f, (b) N 1s, and (c) O 1s of the Ta_3N_5 and Ta_3N_5/NiO_x samples. (d) Ni $2p_{3/2}$ of the Ta_3N_5/NiO_x sample.

shows the presence of oxygen species for both Ta_3N_5 and Ta_3N_5/NiO_x indicating some oxidation of Ta_3N_5. For the coated sample, the Ni $2p_{3/2}$ region clearly shows the presence of Ni mainly associated with NiO_x-type species. From the XPS data, the NiO_x film thickness is estimated to be in the subnanometer range (see Supplementary Note 2 for details). Due to the limited attenuation length of the photoelectrons at $h\nu$ = 1800 eV, the NiO_x layer must be thin enough to allow the detection of Ta_3N_5 through both NiO_x and the layers of water vapor and liquid electrolyte during the *operando* AP-XPS experiments.

3.3. *Operando* AP-XPS Measurements of Ta_3N_5 and Ta_3N_5/NiO_x. It has been previously hypothesized that a Fermi-level pinning suppresses the photoactivity as band bending in the space charge region is not occurring.[5,14] Below, we present direct evidence of such interfacial phenomena by *operando* AP-XPS investigations on the Ta_3N_5 and Ta_3N_5/NiO_x samples in 1 M KOH under dark and illuminated conditions (Figure 4). A detailed analysis of data handling and assumptions made is given in Supplementary Note 1. The O 1s spectra have been deconvoluted into three components ascribed to oxide formation in the nitride film (~530.8 eV), liquid water (~532.8 eV), and vapor (~535.5 eV). As expected, in both samples, we see a linear dependence between the applied potential and the peak position of the O 1s components from both vapor and liquid water. The slope is approaching −1.0 eV/V for the liquid water component (bulk water), which is expected as its electrochemical potential is constant with respect to the reference electrode.[5] This shows that our measurements were performed with the appropriate ionic and electronic contacts between the PEC cell and the AP-XPS instrument. The slight deviation from the expected value of −1.0 eV/V is also observed in relevant works from the literature,[21] and it can be mainly assigned to ohmic losses through the electrolyte solution (ionic resistance).

Under dark conditions, the Ta $4f_{7/2}$ peak position is independent of the applied potential for both the Ta_3N_5 and Ta_3N_5/NiO_x samples. This is a direct evidence of Fermi-level pinning in Ta_3N_5 at the Ta_3N_5/electrolyte and Ta_3N_5/NiO_x interfaces.[5,21] This corroborates well with the *ex situ* findings by He et al., and it also suggests the presence of in-gap states in the Ta_3N_5 films in the potential range probed in these measurements.[14,26] Under illumination and applied bias, the Ta_3N_5 sample shows the same independence of the Ta $4f_{7/2}$ peak position as in the dark. This is in agreement with the low photocurrent density observed during the *operando* AP-XPS measurements. The Fermi-level pinning prevents band bending toward the Ta_3N_5/electrolyte. This means that there is no potential drop in the SCR that can promote the separation of photogenerated holes and electrons, which leads to poor PEC performance. For the NiO_x-coated sample, on the other hand, a negative shift in the Ta $4f_{7/2}$ peak position for an increasing bias is observed under illumination. The Ta $4f_{7/2}$ BE changes by 0.57 eV as the applied bias is varied by 0.85 V in total (from 0.60 to 1.45 V vs RHE), implying increased surface band bending of Ta_3N_5. The shift in BE is reversible when going back to 0.60 V versus RHE, and we see no clear oxidation of the Ta_3N_5. Correspondingly, the NiO_x-coated sample also shows significantly larger photocurrents (factor of 2 at 1.23 V vs RHE), i.e., better separation of photogenerated charges (Figure S5). The PEC performance of the Ta_3N_5/NiO_x sample was stable throughout the AP-XPS acquisition, which exceeded 5 h for all of the studied conditions in total.

https://doi.org/10.1021/acscatal.3c02423
ACS Catal. 2023, 13, 11762−11770

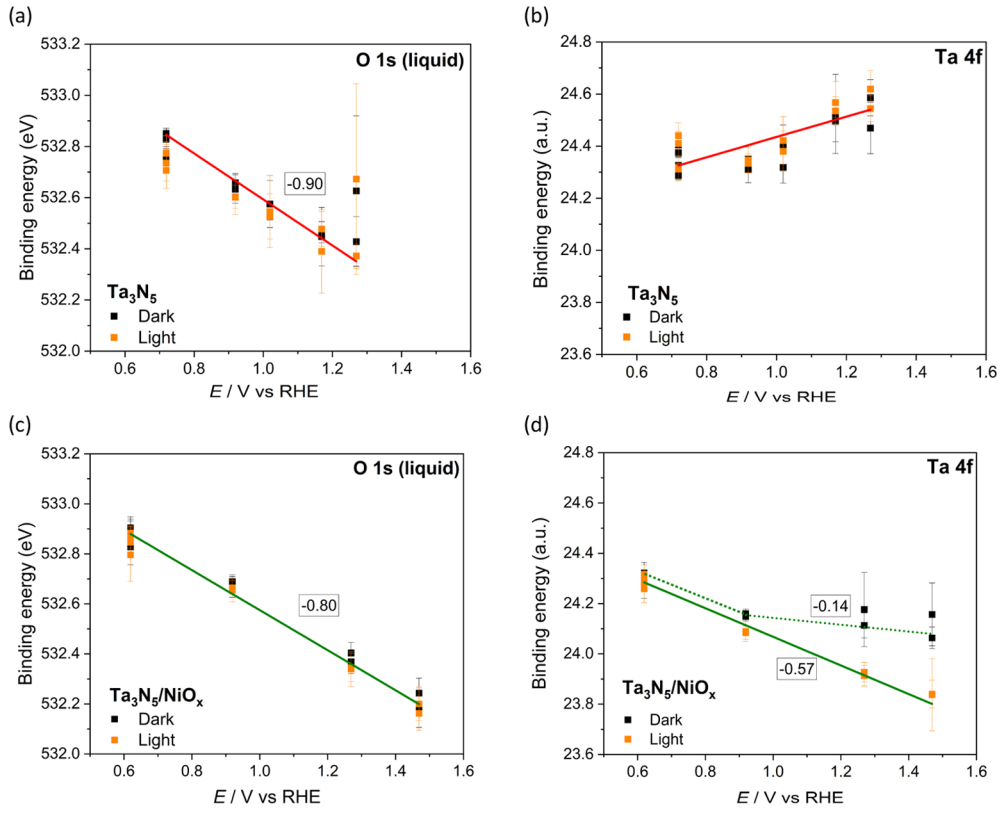

Figure 4. Binding energy of the Ta $4f_{7/2}$ component and liquid contribution in the O 1s spectra during *operando* AP-XPS measurements for (a) and (b) Ta_3N_5 and (c) and (d) Ta_3N_5/NiO_x. Black and yellow markers represent measurements under dark and illuminated conditions, respectively. The current−voltage curves during *operando* AP-XPS can be seen in Figure S5. The PEC measurements in the AP-XPS chamber were conducted in 1 M KOH, Ag/AgCl (3.4 M KCl, liquidless) as the reference electrode, and a Pt sheet (2 cm^2) as the counter electrode. Raw AP-XPS data can be found in Figures S6 and S7.

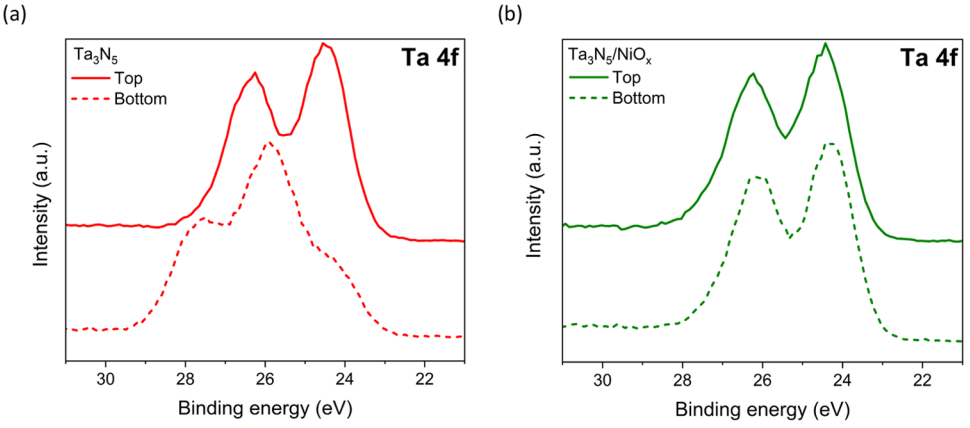

Figure 5. (a) Postoperation XPS measurements under vacuum conditions of used (a) Ta_3N_5 and (b) Ta_3N_5/NiO_x. Dashed lines (labeled: bottom) are measured on areas that were immersed in the electrolyte during the *operando* AP-XPS measurements, and solid lines (labeled: top) are from areas that were not in contact with the electrolyte. The latter areas are considered as unused Ta_3N_5 and Ta_3N_5/NiO_x samples.

3.4. Post-AP-XPS Characterizations of Ta_3N_5 and Ta_3N_5/NiO_x. XPS analyses of the same Ta_3N_5 and Ta_3N_5/NiO_x samples after the *operando* AP-XPS experiments (referred to as "used" Ta_3N_5 and Ta_3N_5/NiO_x) show a striking difference in sample oxidation, as seen in Figure 5a,b. The Ta 4f spectra were taken from the bottom (dashed line, immersed in the electrolyte during AP-XPS) and top (solid line, not immersed in the electrolyte) of the used samples. The top regions of the used samples have Ta 4f spectra similar to those of as-prepared Ta_3N_5 without significant traces of surface degradation/oxidation. For the bottom region of the Ta_3N_5 and Ta_3N_5/NiO_x samples used, however, the difference is remarkable. The appearance of a spin−orbit pair of peaks at higher binding energy (25.8 and 27.7 eV BE, respectively), corresponding to the formation of Ta oxide, is clearly seen in the uncoated sample, while the NiO_x-coated sample shows no evident signs of oxidation for similar operation time and conditions during the AP-XPS measurements. This is shown in more spatial detail in Figure S8, where a linear XPS scan was conducted on a representative used Ta_3N_5 sample.

https://doi.org/10.1021/acscatal.3c02423
ACS Catal. 2023, 13, 11762−11770

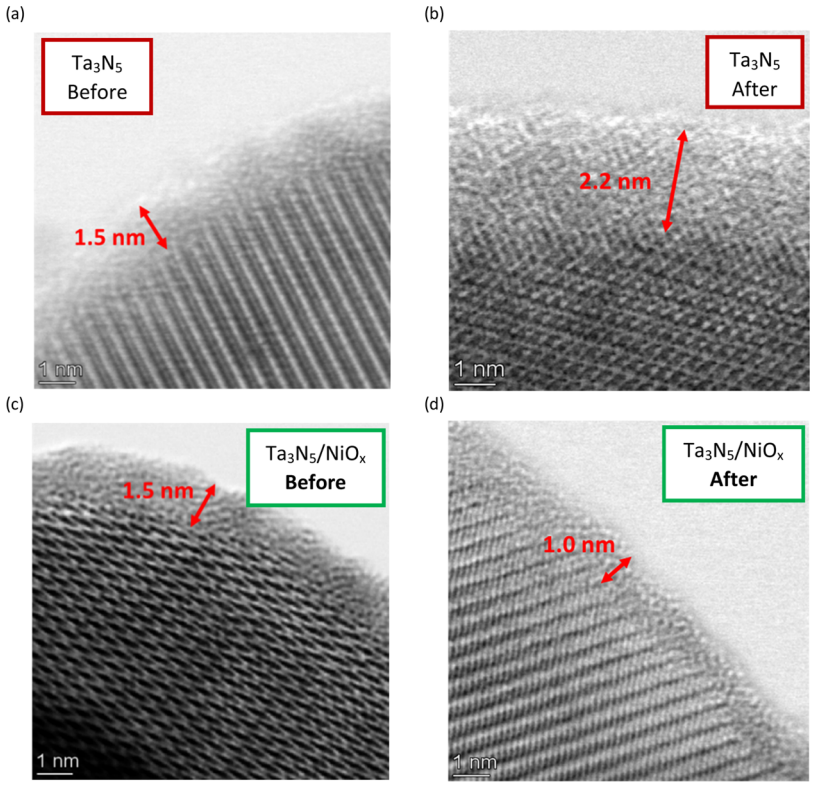

Figure 6. Bright-field STEM images of (a) and (c) Ta_3N_5 and Ta_3N_5/NiO_x before AP-XPS and (b) and (d) after AP-XPS. The thickness of the amorphous surface layer is given in each image. Additional STEM images can be seen in Figure S10.

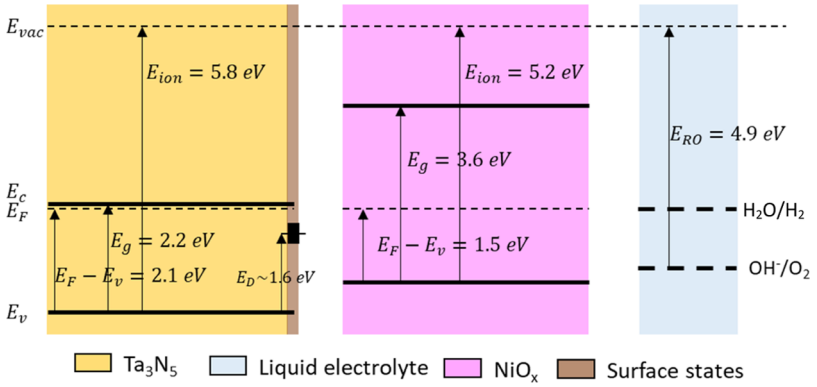

Figure 7. Band structure of the separate phases Ta_3N_5 (left), NiO_x (middle), and liquid alkaline electrolyte (right). For the electrolyte band structure, literature values have been used and corrected for 1 M KOH and a pH of 14.[27]

TEM investigations from the areas of the Ta_3N_5 and Ta_3N_5/NiO_x samples that were not immersed in the electrolyte are given in Figure 6a,b. The bright-field STEM images reveal a porous structure of both Ta_3N_5 films with thin amorphous surface layers of about 1.5 nm in thickness. The large Ta_3N_5 surface roughness makes it difficult to observe the NiO_x coating, which was found by XPS to be very thin (<1 nm). Thicker NiO_x layers of ~7 nm were grown on both Si and Ta_3N_5 substrates to visualize their morphology. TEM investigations of these can be found in Figure S9, where it is seen that the coating is a layer of NiO_x nanocrystals covering the substrate surface.

Post-AP-XPS operation STEM analysis of the Ta_3N_5 and Ta_3N_5/NiO_x samples in regions that were immersed in the electrolyte solution vividly shows the effect of the NiO_x, which clearly suppresses further amorphization, as seen in Figure 6b,d for used Ta_3N_5 and Ta_3N_5/NiO_x samples, respectively. Importantly, the amorphous layer at the surface of the used Ta_3N_5 film has grown thicker (refer to Figures 6a,b and S10a–c), while it stays constant for the used Ta_3N_5/NiO_x sample (refer to Figures 6c,d and S10d–f). Figure S11 shows EDS scan lines of the oxygen concentration at these four cross-sectional images, showing that the used Ta_3N_5 film has significantly more oxygen. This indicates that the thicker amorphous layer of Ta_3N_5 (Figure 6b) is more oxygen-rich than that in the case of the used Ta_3N_5/NiO_x sample, consistent with the XPS results presented in Figure 5a.

4. DISCUSSION

Our AP-XPS results indicate pinning of the E_F of the Ta_3N_5/electrolyte,[5,21] both when the semiconductor is in direct contact with the electrolyte (dark and light conditions) and

https://doi.org/10.1021/acscatal.3c02423
ACS Catal. 2023, 13, 11762−11770

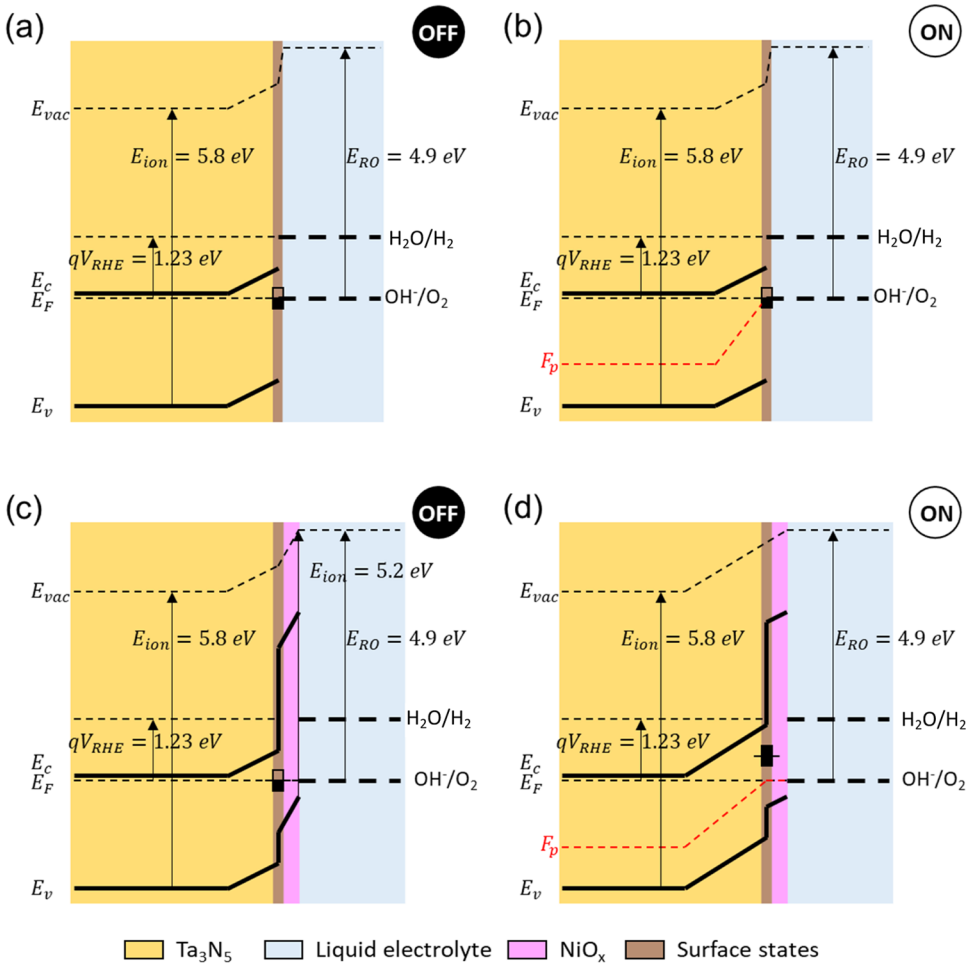

Figure 8. Band energy diagrams of (a, b) the Ta_3N_5/electrolyte under dark and illumination conditions, respectively, and (c, d) Ta_3N_5/NiO_x/electrolyte in the dark and under illumination, respectively. The ionization energies for Ta_3N_5 and NiO_x were obtained by UPS and are reported in eV.

when it is protected/passivated by NiO_x (Ta_3N_5/NiO_x/electrolyte, only the dark condition). Interestingly, unpinning of the E_F is observed in the illuminated Ta_3N_5/NiO_x/electrolyte heterojunction, accompanied by the generation of a significant photocurrent. To further understand the mechanism(s) causing the observed pinning and unpinning of E_F, we have measured the ionization energies for Ta_3N_5 and NiO_x thin films with UPS (see Figure S12 and Table S2 and details therein) and sketched the initial electron energy bands before the formation of the two distinct heterojunctions, i.e., Ta_3N_5/electrolyte and Ta_3N_5/NiO_x/electrolyte (Figure 7).

The equilibrium between the Ta_3N_5 electrode and the OH^-/O_2 redox level of the electrolyte, as illustrated in Figure 8a, requires charge transport and buildup of an electrostatic potential difference over the junction (interface) until the E_F of Ta_3N_5 is aligned with the redox potential involved in the charge transfer (assumed to be OH^-/O_2 in Figure 8). The existence of defect levels at ~1.6 eV above the valence band edge has been previously documented by Fu et al.[15] and attributed to N vacancies and reduced Ta states (Ta^{3+}). The concentration of such defects is expected to be present in increased amounts at the surface. Such defect levels will be filled by electrons and charge-neutralized if the Fermi level is above the defect level. As the band bending shifts the defect level toward the Fermi level, the defect level becomes only partially filled by electrons and hence positively charged. This surface charge density contributes to the electrostatic potential in the same manner as the space charge region, and for high defect density, the Fermi level is pinned to the defect level. As the electric biasing of the junction is varied, the filling of the defect level changes considerably with only a small variation in the band bending. With this Fermi-level pinning, the Ta $4f_{7/2}$ BE will not change with the potential in the *operando* AP-XPS PEC measurements. We also observe a significant positive dark current at 0.90 V < E < 1.23 V vs RHE (Figure 2). This is not from oxygen evolution and can be attributed to oxidation of the Ta_3N_5 electrode. Indeed, we see a slight increase in the Ta $4f_{7/2}$ BE at these potentials (Figure 4b), consistent with the oxidation of Ta_3N_5 to TaO_xN_y, as observed by our post-operation characterizations (Figures 5, 6, and S8). Under illumination, we see the same behavior of the Ta $4f_{7/2}$ BE as in the dark and only a modest photocurrent. The defect level facilitates a rapid electron/hole recombination in the surface region, resulting in a low hole density near the interface and a low photocurrent. This is illustrated in Figure 8b by the large distance between the hole quasi-Fermi level (F_p) and the valence band edge at the interface. Such defect levels, where charge is accumulated, promote the degradation of the material through self-oxidation (anodic potentials) or reduction (cathodic potentials) in aqueous media.[18,23]

https://doi.org/10.1021/acscatal.3c02423
ACS Catal. 2023, 13, 11762−11770

The energy band lineup for the Ta_3N_5/NiO_x/electrolyte junction under equilibrium conditions is illustrated in Figure 8c. The discontinuity of the valence and conduction band edges across the Ta_3N_5/NiO_x interface is expected based on the UPS measurements of the ionization energies of Ta_3N_5 and NiO_x (and their band gaps). The suppressed dark current, compared to the Ta_3N_5 electrode, shows that the NiO_x efficiently protects Ta_3N_5 from oxidation, and we do not observe an increase in the Ta $4f_{7/2}$ BE in the *operando* AP-XPS PEC measurements in the potential range $0.90 < E < 1.23$ V vs RHE. Under illumination, a significant (and stable) photocurrent is generated. We also observe a decrease in the Ta $4f_{7/2}$ BE with increasing potential versus RHE showing an increasing positive band bending and unpinning of the Fermi level (Figure 8d). The valence band discontinuity between Ta_3N_5 and NiO_x facilitates hole transport from Ta_3N_5 to NiO_x and the NiO_x also increases the reaction kinetics for the OER,[28] observed as stable photocurrent generation (Figure S5). This alters the electron filling of the defect states. Since the holes are rapidly transported away from the Ta_3N_5 surface, the recombination rate for electrons trapped in the defect states is reduced, increasing the electron filling of defect states under illumination, ultimately passivating them, and, at the same time, unpinning the quasi-Fermi levels.

5. CONCLUSIONS

In this work, we probed the semiconductor/electrolyte interfacial energetics in the presence of applied bias under dark and illumination conditions by *operando* AP-XPS. The model system was based on a Ta_3N_5 film with or without a subnanometer protective/passivating and catalytically active layer of ALD-coated NiO_x. This study unraveled that surface passivation of defect states, which are responsible for Fermi-level pinning in Ta_3N_5, can suppress the recombination of photogenerated carriers by allowing an unpinning of the quasi-Fermi level of the photogenerated holes (for n-type materials such as Ta_3N_5). We expect a similar behavior for the case of p-type photocatalysts, a major finding toward the stabilization of photocatalytic materials under harsh operating conditions for the demonstration of viable systems of water photoelectrolysis.

■ ASSOCIATED CONTENT

Supporting Information

The Supporting Information is available free of charge at https://pubs.acs.org/doi/10.1021/acscatal.3c02423.

Additional experimental details, supporting figures including electrode schematics, STEM images, EDS-STEM measurements, transmittance measurements, XRD, photocurrent−voltage curves recorded during operando AP-XPS, raw AP-XPS data, UPS spectra, and supplementary tables and supplementary notes (PDF)

■ AUTHOR INFORMATION

Corresponding Authors

Ingvild Julie Thue Jensen − *SINTEF Industry, NO-0373 Oslo, Norway*; orcid.org/0000-0002-8575-0171; Email: ingvildjuliethue.jensen@sintef.no

Athanasios Chatzitakis − *Centre for Materials Science and Nanotechnology, Department of Chemistry, University of Oslo, NO-0349 Oslo, Norway*; orcid.org/0000-0001-7193-3236; Email: athanasios.chatzitakis@smn.uio.no

Authors

Øystein Dahl − *SINTEF Industry, NO-7465 Trondheim, Norway*

Martin Fleissner Sunding − *SINTEF Industry, NO-0373 Oslo, Norway*

Veronica Killi − *Centre for Materials Science and Nanotechnology, Department of Chemistry, University of Oslo, NO-0349 Oslo, Norway*

Ingeborg-Helene Svenum − *SINTEF Industry, NO-7465 Trondheim, Norway*

Mathieu Grandcolas − *SINTEF Industry, NO-0373 Oslo, Norway*

Magnus Andreassen − *Centre for Materials Science and Nanotechnology, Semiconductor Physics, Department of Physics, University of Oslo, NO-0349 Oslo, Norway*; orcid.org/0009-0001-8221-8593

Ola Nilsen − *Centre for Materials Science and Nanotechnology, Department of Chemistry, University of Oslo, NO-0349 Oslo, Norway*; orcid.org/0000-0002-2824-9153

Annett Thøgersen − *SINTEF Industry, NO-0373 Oslo, Norway*

Complete contact information is available at: https://pubs.acs.org/10.1021/acscatal.3c02423

Notes

The authors declare no competing financial interest.

■ ACKNOWLEDGMENTS

The authors acknowledge support from the Research Council of Norway through the SolOPP project (315032) and the national infrastructures National Surface and Interface Characterisation Laboratory, NICE (195565), the Norwegian Center for Transmission Electron Microscopy, NORTEM (197405), and the Norwegian Micro- and Nano-Fabrication Facility, NorFab (295864). The authors acknowledge MAX IV Laboratory for time on Beamline HIPPIE under Proposal 20210982. The authors would like to thank R. Temperton and A. Shavorskiy for assistance with the experiment. Research conducted at MAX IV, a Swedish national user facility, is supported by the Swedish Research Council under contract 2018-07152, the Swedish Governmental Agency for Innovation Systems under contract 2018-04969, and Formas under contract 2019-02496.

■ REFERENCES

(1) Fujishima, A.; Honda, K. *Nature* **1972**, *238*, 37−38.

(2) Yang, W.; Prabhakar, R. R.; Tan, J.; Tilley, S. D.; Moon, J. *Chem. Soc. Rev.* **2019**, *48*, 4979−5015.

(3) Jiang, C.; Moniz, S. J. A.; Wang, A.; Zhang, T.; Tang, J. *Chem. Soc. Rev.* **2017**, *46*, 4645−4660.

(4) Zhu, S.; Scardamaglia, M.; Kundsen, J.; Sankari, R.; Tarawneh, H.; Temperton, R.; Pickworth, L.; Cavalca, F.; Wang, C.; Tissot, H.; Weissenrieder, J.; Hagman, B.; Gustafson, J.; Kaya, S.; Lindgren, F.; Kallquist, I.; Maibach, J.; Hahlin, M.; Boix, V.; Gallo, T.; Rehman, F.; D'Acunto, G.; Schnadt, J.; Shavorskiy, A. *J. Synchrotron Radiat.* **2021**, *28*, 624−636.

(5) Lichterman, M. F.; Hu, S.; Richter, M. H.; Crumlin, E. J.; Axnanda, S.; Favaro, M.; Drisdell, W.; Hussain, Z.; Mayer, T.; Brunschwig, B. S.; Lewis, N. S.; Liu, Z.; Lewerenz, H.-J. *Energy Environ. Sci.* **2015**, *8*, 2409−2416.

(6) Hu, S.; Richter, M. H.; Lichterman, M. F.; Beardslee, J.; Mayer, T.; Brunschwig, B. S.; Lewis, N. S. *J. Phys. Chem. C* **2016**, *120*, 3117−3129.

(7) Axnanda, S.; Crumlin, E. J.; Mao, B.; Rani, S.; Chang, R.; Karlsson, P. G.; Edwards, M. O. M.; Lundqvist, M.; Moberg, R.; Ross, P.; Hussain, Z.; Liu, Z. *Sci. Rep.* **2015**, *5*, No. 9788.
(8) Temperton, R. H.; Kawde, A.; Eriksson, A.; Wang, W.; Kokkonen, E.; Jones, R.; Gericke, S. M.; Zhu, S.; Quevedo, W.; Seidel, R.; Schnadt, J.; Shavorskiy, A.; Persson, P.; Uhlig, J. *J. Chem. Phys.* **2022**, *157*, 244701 DOI: 10.1063/5.0130222.
(9) Xu, K.; Chatzitakis, A.; Jensen, I. J. T.; Grandcolas, M.; Norby, T. *Photochem. Photobiol. Sci.* **2019**, *18*, 837−844.
(10) Chun, W.-J.; Ishikawa, A.; Fujisawa, H.; Takata, T.; Kondo, J. N.; Hara, M.; Kawai, M.; Matsumoto, Y.; Domen, K. *J. Phys. Chem. B* **2003**, *107*, 1798−1803.
(11) Xu, K.; Chatzitakis, A.; Risbakk, S.; Yang, M.; Backe, P. H.; Grandcolas, M.; Bjørås, M.; Norby, T. *Catal. Today* **2021**, *361*, 57−62.
(12) Xu, K.; Chatzitakis, A.; Backe, P. H.; Ruan, Q.; Tang, J.; Rise, F.; Bjørås, M.; Norby, T. *Appl. Catal., B* **2021**, *296*, No. 120349.
(13) Liu, G.; Ye, S.; Yan, P.; Xiong, F.; Fu, P.; Wang, Z.; Chen, Z.; Shi, J.; Li, C. *Energy Environ. Sci.* **2016**, *9*, 1327−1334.
(14) He, Y.; Thorne, J. E.; Wu, C. H.; Ma, P.; Du, C.; Dong, Q.; Guo, J.; Wang, D. *Chem* **2016**, *1*, 640−655.
(15) Fu, J.; Wang, F.; Xiao, Y.; Yao, Y.; Feng, C.; Chang, L.; Jiang, C.-M.; Kunzelmann, V. F.; Wang, Z. M.; Govorov, A. O.; Sharp, I. D.; Li, Y. *ACS Catal.* **2020**, *10*, 10316−10324.
(16) Kawase, Y.; Higashi, T.; Katayama, M.; Domen, K.; Takanabe, K. *ACS Appl. Mater. Interfaces* **2021**, *13*, 16317−16325.
(17) Wang, P.; Fu, P.; Ma, J.; Gao, Y.; Li, Z.; Wang, H.; Fan, F.; Shi, J.; Li, C. *ACS Catal.* **2021**, *11*, 12736−12744.
(18) Fu, J.; Fan, Z.; Nakabayashi, M.; Ju, H.; Pastukhova, N.; Xiao, Y.; Feng, C.; Shibata, N.; Domen, K.; Li, Y. *Nat. Commun.* **2022**, *13*, No. 729.
(19) Zhao, Y.; Liu, G.; Wang, H.; Gao, Y.; Yao, T.; Shi, W.; Li, C. *J. Mater. Chem. A* **2021**, *9*, 11285−11290.
(20) Lindahl, E.; Ottosson, M.; Carlsson, J.-O. *Chem. Vap. Deposition* **2009**, *15*, 186−191.
(21) Shavorskiy, A.; Ye, X.; Karslıoğlu, O.; Poletayev, A. D.; Hartl, M.; Zegkinoglou, I.; Trotochaud, L.; Nemšák, S.; Schneider, C. M.; Crumlin, E. J.; Axnanda, S.; Liu, Z.; Ross, P. N.; Chueh, W.; Bluhm, H. *J. Phys. Chem. Lett.* **2017**, *8*, 5579−5586.
(22) Higashi, T.; Nishiyama, H.; Nandal, V.; Pihosh, Y.; Kawase, Y.; Shoji, R.; Nakabayashi, M.; Sasaki, Y.; Shibata, N.; Matsuzaki, H.; Seki, K.; Takanabe, K.; Domen, K. *Energy Environ. Sci.* **2022**, *15*, 4761−4775.
(23) Li, K.; Miao, B.; Fa, W.; Chen, R.; Jin, J.; Bevan, K. H.; Wang, D. *ACS Appl. Mater. Interfaces* **2021**, *13*, 17420−17428.
(24) Zhen, C.; Chen, R.; Wang, L.; Liu, G.; Cheng, H.-M. *J. Mater. Chem. A* **2016**, *4*, 2783−2800.
(25) Khan, S.; Teixeira, S. R.; Santos, M. J. L. *RSC Adv.* **2015**, *5*, 103284−103291.
(26) Harb, M.; Basset, J.-M. *J. Phys. Chem. C* **2020**, *124*, 2472−2480.
(27) Smith, W. A.; Sharp, I. D.; Strandwitz, N. C.; Bisquert, J. *Energy Environ. Sci.* **2015**, *8*, 2851−2862.
(28) Roger, I.; Shipman, M. A.; Symes, M. D. *Nat. Rev. Chem.* **2017**, *1*, 0003.

https://doi.org/10.1021/acscatal.3c02423
ACS Catal. 2023, 13, 11762−11770